Journal of Electronic Imaging

JElectronicImaging.org

Three-dimensional reconstruction of Roman coins from photometric image sets

Lindsay MacDonald
Vera Moitinho de Almeida
Mona Hess

SPIE. IS&T imaging.org

Lindsay MacDonald, Vera Moitinho de Almeida, Mona Hess, "Three-dimensional reconstruction of Roman coins from photometric image sets," *J. Electron. Imaging* **26**(1), 011017 (2017), doi: 10.1117/1.JEI.26.1.011017.

Journal of Electronic Imaging 26(1), 011017 (Jan/Feb 2017)

Three-dimensional reconstruction of Roman coins from photometric image sets

Lindsay MacDonald,[a,*] Vera Moitinho de Almeida,[b] and Mona Hess[a]
[a]University College London, Department of Civil, Environmental and Geomatic Engineering, Chadwick Building, Gower Street, London WC1E 6BT, United Kingdom
[b]Universitat Autònoma de Barcelona (UAB), Department of Prehistory, Quantitative Archaeology Lab (LAQU), Edifici B Facultat de Filosofia i Lletres, Bellaterra, Barcelona 08193, Spain

Abstract. A method is presented for increasing the spatial resolution of the three-dimensional (3-D) digital representation of coins by combining fine photometric detail derived from a set of photographic images with accurate geometric data from a 3-D laser scanner. 3-D reconstructions were made of the obverse and reverse sides of two ancient Roman denarii by processing sets of images captured under directional lighting in an illumination dome. Surface normal vectors were calculated by a "bounded regression" technique, excluding both shadow and specular components of reflection from the metallic surface. Because of the known difficulty in achieving geometric accuracy when integrating photometric normals to produce a digital elevation model, the low spatial frequencies were replaced by those derived from the point cloud produced by a 3-D laser scanner. The two datasets were scaled and registered by matching the outlines and correlating the surface gradients. The final result was a realistic rendering of the coins at a spatial resolution of 75 pixels/mm (13-μm spacing), in which the fine detail modulated the underlying geometric form of the surface relief. The method opens the way to obtain high quality 3-D representations of coins in collections to enable interactive online viewing. © *2017 SPIE and IS&T* [DOI: 10.1117/1.JEI.26.1.011017]

Keywords: three dimension; surface normals; photometric stereo; three-dimensional laser scanning; coins; numismatics.

Paper 16465SS received Jun. 1, 2016; accepted for publication Nov. 14, 2016; published online Feb. 3, 2017.

1 Introduction and State-of-the-Art Review

1.1 *Coins of Diva Faustina*

In the European research network "Color and Space in Cultural Heritage" (COSCH), a collaborative study has been conducted from 2014 to 2016 to apply various three-dimensional (3-D) techniques to record two ancient Roman coins, to compare their features and properties, and to assess the metric accuracy and effectiveness of the techniques for visualization and conservation assessment. The coins, silver denarii from the period of Antoninus Pius (138 to 161 AD), pose considerable challenges for 3-D recording because of their small size and their material and surface properties. The study aims to demonstrate the value of digital recording techniques for numismatic collections, which continue to rely on traditional documentation, such as two-dimensional (2-D) photography. In particular, it seeks a better understanding of the surface characteristics of historic coins and their measurements, from which cross-sectional profiles and shape may be determined. These are of great interest to numismatists as aids to identifying the die type and date of production.

On the same day that she died in 140 AD, Faustina was named a "diva" by the Senate at the behest of her husband, the Emperor Antoninus Pius, and her death had an unprecedented impact on the religious life and physical fabric of Rome.[1] She was consecrated and thereby granted formal immortality, a priesthood was assigned to her worship, a temple and altar were dedicated to her, her image was carried in the procession (*pompa circensis*) that preceded the official games at religious festivals, and a foundation for orphan girls was established in her honor.

Coins in the name of "Diva Faustina" were issued in great profusion throughout the whole reign of Antoninus Pius, and the coinage of Diva Faustina was the most varied of all Roman posthumous series. Based on evidence from various hoards, it has been estimated that 30% of all gold coinage and 39% of all silver coinage minted during the 20 further years of the reign of Antoninus Pius was "female," i.e., with the head of Faustina on the obverse.[2] On the reverse of these coins, Faustina was represented by a series of divine personifications, under the guise of goddesses, such as Juno, Ceres, Vesta, and Aeternitas.[3] The silver denarii are notably different from the "male denarii" of the same period.[4] What also makes the Faustina coinage unique is that her designs evolved over the 20-year period separately from those of the emperor and show great typological variety and novelty.

Two silver denarii depicting Diva Faustina were chosen as the test objects for the COSCH study (Fig. 1). The two study coins are not part of a collection or museum. As Diva Faustina coins are still widely available for coin collectors in auctions, coin A stems from private ownership (2006) and coin B from a coin dealer with a certificate of provenance.

The obverse of both coins shows the bust of the empress, facing right, with the raised inscription DIVΛ FΛUSTINΛ, but they appear to be the work of different artists as the portrayal on coin A is rather more flattering. Both show her distinctive hair style, with braided locks pinned up at the back of her head. The designs on the reverse are different: coin A shows Aeternitas holding a globe in her right hand, with

*Address all correspondence to: Lindsay MacDonald, E-mail: lindsay.macdonald@ucl.ac.uk

1017-9909/2017/$25.00 © 2017 SPIE and IS&T

Fig. 1 Obverse and reverse of two silver Roman denarii depicting Diva Faustina. Coin A is on the left and Coin B on the right. The images were taken by a Nikon D200 camera using a single flash light to the upper left at an elevation of ~60 deg.

palla billowing out around her head, inscription ΛETER-NITΛS; coin B shows Vesta, holding the palladium in her right hand, scepter in her left, inscription VES-TΛ. Each coin is between 17.5 and 18.0 mm in diameter and ~1.5 mm in thickness.

1.2 *Photography of Coins*

Documentation is "essential in the practice of conservation."[5] Codes of ethics typically call for application of the "highest possible standard" to "written and pictorial records" as part of "the diagnostic examination and recording of an object."[6] This applies to coin collections like all other cultural heritage objects, material culture, and archives.

Coins found on archaeological sites are typically documented by manual drawings (Fig. 2) and photographs. This has been considered necessary because the finds generally have signs of wear, dirt, corrosion, and so on. Finds often have to be documented properly, because they cannot legally be taken outside the country hosting the excavation.[7]

The study of a coin's features has traditionally been conducted by direct hands-on examination, employing magnification tools and a strong directional light source. By holding the coin under the light and tilting it relative to the viewing direction, the surface features may be discerned. The quality of numismatic information that can be gleaned from a coin decreases further if in-person examination is not possible. Traditional photographic images convey only a subset of the information discernible through direct physical inspection.[8]

In the documentation of coins, photographs provide additional information besides the written description, conveying both the visual design and the state of preservation. Traditionally, coins have been photographed by numismatists as 2-D monochrome images, and these are of great qualitative value. But unless a standardized configuration of illumination is employed, it is difficult to use the images for quantitative analysis and comparison. For imaging of premodern coins, for example, numismatic photographers have sometimes employed a light source inclined at an angle from the optical axis of the camera. This has the advantage of reducing the direct specular reflections from the metallic surface, but it produces bright reflections from gradients on one side of relief features and shadows on the other (see Fig. 1). This asymmetrical rendering, which depends on both illumination and viewing angles, makes it difficult to decide whether a coin was minted by the same die. In general, the intensity, direction, and number of light sources may vary from one studio to another, leading to differences in the shadows cast, the contrast between bright and dark regions, and the rendering of surface texture. Different lighting directions may make small patterns on the coin, such as inscriptions and symbols, look very different, and highlights arising from specularity of the metallic surface may affect the quality of the images. The use of polarizing filters to reduce specular highlights can cause undesirable birefringence effects.[8] More fundamentally, the projection of the object relief onto the image plane means that valuable information about the object is discarded, which makes it more difficult to analyze distortions arising from the striking of the coin in the die and also of subsequent wear and corrosion.[9]

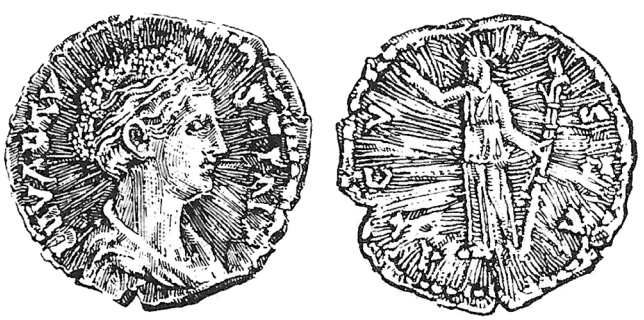

Fig. 2 Numismatic drawing of a Roman denarius depicting Faustina the Elder, from Hoberman (1981), page 88. The radiating stress marks on both sides of this specimen were caused by imperfect striking.

Because of the relatively small size, shallow relief, and metallic specularity of most coins, special techniques are needed for photography. In addition to a copystand and macro lens, careful attention needs to be paid to the geometry of the incident illumination. Raised areas of the surface need to be rendered in the image by tones different from those of the ground plane of the coin. This cannot be achieved in most cases by a single light source at an oblique angle, as in Fig. 1, because for a shiny surface, the light is reflected away from the camera, making it appear too dark. Moreover, the reflection from the leading edge of each surface feature becomes an overexposed specular highlight, while the trailing edge is cast into shadow. The resulting image is harsh in contrast, the gradients are strongly directional, and fine surface texture may be exaggerated.

Hoberman, writing in the days of analog photography recommended axial illumination with an umbrella reflector to reproduce maximum gradation of tone and to record subtle hue variations.[10] A traditional technique used by professionals is to illuminate the coin through a periscope arrangement, in which the camera views it through a plate of glass or a half-silvered mirror.[11] Only rays reflected parallel to the optical axis are captured, resulting in an image that is light in horizontal surfaces of the coin and dark in inclined

surfaces, i.e., the outlines of relief features. Conversely, a different apparatus with a white paper cone enables the sloping sides of features to be illuminated without frontal light, resulting in light outlines and dark surfaces.

Goodman notes that illumination from an angle as near as possible to axial improves the relief, helps to prevent dark spots, makes the details more vibrant, and enhances the luster.[12] Single lights, especially those closer to a point source, produce high contrast in the image. He distinguishes between three classes of coins, according to their degree of metallic specularity, corresponding to normal coins in circulation (low contrast), new coins (medium contrast), and brilliant proof coins (high contrast). For these, he recommends illumination by one, two, and three lights, respectively, adding a diffused light where needed to soften the shadows in the image.

1.3 *Image Processing of Coins in Two-Dimension*

Because coins are the artifacts most frequently preserved throughout all historical periods, their study and documentation can lead to a new understanding of history. Numismatic research can show not only where a particular coin was minted, but also how a coin type has developed over time. It is of great importance to numismatists to have tools that reduce the effort of analysis and the complexity of identifying coins from identical dies.[13]

There is a substantial body of literature on the processing of 2-D digital images of coins for classification and identification.[14] Methods for image-based recognition of modern coins include artificial neural networks, edge features, gradient directions, eigenspaces and color, shape, and wavelet features.[15] Additional approaches have been used for classifying ancient coins using scale-invariant feature transform (SIFT) features.[16] Good results have been achieved with a generalized Hough transform to segment the coin edges and features.[17,18] A method called deviation from circular shape was shown to facilitate matching of the irregular shapes of ancient coins by a linear combination of local and global shape techniques, in which the local matching was based on the difference of Fourier shape descriptors, whereas the correlation coefficient between the curves served as a global measure of shape similarity.[19]

Image processing methods have also been applied to identify and retrieve coins stolen from excavations due to their value for collectors. The system developed in the project "Combat On-line Illegal Numismatic Sales (COINS)" was tested on a dataset provided by the Fitzwilliam Museum, Cambridge, consisting of 2400 images of 240 different coins, recorded in varying view positions by means of different rotations on both reverse and obverse sides. Independently of shape and local features, the system achieved an identification rate of 95.2%.[15] For the MUSCLE CIS benchmark competition, a new coin dataset was developed containing ~100,000 coin images. The dataset was divided into a fixed training set of 20,000 coins, and six fixed test sets of 5,000 coins, with both obverse and reverse of each coin. The training set contained 2270 different coin faces, corresponding to 692 coin classes. In the test sets, ~400 of the coin classes appeared, and, in addition, the test set contained 3% to 4% of coins not in the training set, which should be classified as unknown.[20]

1.4 *Three-Dimensional Imaging of Coins*

3-D imaging technology allows nondestructive, noninvasive recording of the surface to construct a virtual image of the real object, i.e., a 3-D model. Research with cultural heritage professionals has confirmed the relevance of 3-D imaging and established that, by creating accurate geometric representations, user motivations can be addressed for surface measurement and inspection, deformation monitoring, and 3-D printing.[21,22] Cross-sections, surface heights, and profiles can be extracted from the dataset.[7] 3-D digital documentation may, therefore, be of great value to identify deterioration or damage, for example, before and after loan. In education, "object-based learning" sessions increasingly include 3-D digital representations to stimulate student interaction.[23]

Very little research has been done to date on 3-D imaging of coins or their processing. 3-D models for 22 historical coins digitized by a 3-D structured light scanner (SLS) were compared for diameter and volume against manually measured values, giving coefficients of variation of 1.23% and 0.26%, respectively.[24] The volume is relevant for calculation of the density of the coin to identify differences between the theoretical and actual densities when coins were plated, for instance, with silver over a copper core. Interactive 3-D models help numismatists to recognize coins because the models, like the originals, can be viewed and analyzed from any viewpoint and in any scale. Another important feature is that 3-D models show the difference between the axes of the obverse and reverse faces, which are not necessarily aligned for ancient and medieval coins because they were hammered, not cast.[14]

One of the disadvantages of laser-based 3-D scanning systems is that they are generally limited in spatial resolution, with a typical sampling pitch, or ground sampling distance (GSD), of 100 μm, corresponding to 10 points/mm on the surface of the object. As a general rule, in accordance with the Nyquist sampling criterion, the inter-point distance should be at most half the size of the smallest feature of the object that is required to be discernible in the digital representation. The finest feature that can be resolved, therefore, is 0.2 mm or 200 μm. Coins, however, are relatively small in size, with diameters generally in the range 15 to 50 mm, and have very fine surface detail and shallow surface relief. For veridical representation, all spatial detail down to the limit of the human visual system of 40 μm should be captured, requiring a spatial resolution of at least 50 points/mm.[25] Thus, there is a factor of 5 between what is needed and the actual capability of 3-D laser scanners.

1.5 *Reflectance Transform Imaging and Coins*

Systematic photography with directional illumination enables richer documentation of objects because the ensemble of images contains implicit information about the surface relief. This can be exploited through the polynomial texture mapping (PTM) technique,[26] in which a biquadratic function of incident illumination angle is fitted to the vector of intensity values at each pixel. When the reconstructed image is displayed through the interactive viewer software with a moving virtual light source, the illusion of 3-D produced by the interplay of light and shadow is compelling, making it particularly suitable for showing the surface relief of coins. The disadvantage is that because only six parameters are

used in the biquadratic function, the angular distribution is not much more directional than a simple Lambertian, and cannot properly represent the specular components of shiny metallic surfaces. The PTM image can be analyzed to find the most advantageous combination of illumination angle(s) and enhancement effect(s) that illustrate the characteristics under discussion. The parameters can then be saved as part of the descriptive record for the coin, enabling the visualization to be replicated in the future.[8]

PTM is one of a family of methods known as reflectance transform imaging (RTI). Two innovations made it a more versatile technique for a variety of cultural heritage imaging applications.[27] First, by determining the direction of incident illumination from the highlight on a sphere placed within the image frame, it became possible to capture image sets with a movable handheld light source instead of an illumination dome. Second, the implementation of an alternative set of basis functions, known as hemispherical harmonics, provides a better localization of the directionality of the illumination and, therefore, improves the modeling of specular highlights. RTI provides several advantages compared to other close-range 3-D recording techniques for near-flat surfaces: (a) RTI uses inexpensive and widely available and easily transportable hardware (SLR camera, tripod, and flash); (b) RTI scales well for both small and large object dimensions; and (c) RTI can achieve a high sampling density for near-flat surfaces that is only recently achieved by other 3-D imaging techniques, such as laser scanners, structured light scanners or photogrammetric structure from motion (SfM). It also produces a highly detailed, colorimetrically correct, visually attractive and intuitively understandable digital image of the surface of an artifact. For these reasons, RTI techniques have become widely adopted in the cultural heritage field for documentation tools and detailed visual analysis,[27] particularly in the field of archaeology.[28]

An experimental system was used to create PTM representations of Roman and medieval coins from the collection at the monastery of St. Bernard.[8] The system consisted of a template for 24 light positions in a hemispherical array surrounding the coin, a fiber optic directional light source, and a computer-controlled camera. The PTMs were bundled with a Java-based viewer and displayed, with descriptions in French, on the monastery website in order to "allow people to consult some of the seminal objects of our civilization." The study concluded that PTMs provide an interactive experience of a more complete dataset than traditional numismatic documentation and that they offer a more informed method for generating images that convey numismatic ideas.

RTI was also used for presenting a collection of coins for public display through an interactive kiosk at the National Museum of San Matteo in Pisa.[29] The objectives of the project were to enable the virtual manipulation of the coins for detailed inspection, and thereby to reveal their features in an easy and understandable way. The collection includes both gold coins with highly specular surfaces and bronze coins that are more matte and present patinas resulting from various degradation processes. For each face of each coin, a set of 260 images was captured by a CCD camera in an illumination dome from the University of Leuven equipped with 260 white light-emitting diodes.

2 Processing Coin Images: Digital Elevation Map from Photometric Plus 3-D Laser Scanner Data

The present study combined two datasets representing the surface topography of the two Faustina coins (Fig. 1). First, they were scanned by a 3-D color laser scanner, producing a point cloud of the surface shape. Second, they were photographed in an illumination dome with directional lighting. The two representations were combined to produce a digital elevation map (DEM) of each coin with the accuracy of the scanner and the fine detail of the photography. The same method was applied to both the obverse and reverse of each coin, but the illustrations in the following sections are all for the obverse of the Faustina A coin.

2.1 *Coin Outlines from Images*

The dome imaging system at UCL enables sets of images of an object to be taken with illumination from different directions. A hemisphere of 104-cm diameter is fitted with 64 flash lights and calibrated so that the geometric centroid coordinates of every light source are known to within 3.0 mm.[30] A digital camera at the "north pole" captures a series of 64 color images, each illuminated from a different direction and all in pixel register. This enables the object to be visualized from a fixed viewing angle, i.e., vertically from above, for many different angles of incident light.

For photography, the coins were placed on a black cardboard sheet to provide a dark image background free from texture. Each side of each coin was photographed in the dome using a Nikon D200 camera fitted with a Nikkor 200 mm macro lens, achieving a resolution of 75.3 pixels/mm, so that each pixel corresponds to 13 μm on the surface of the coin. The dimensions of each coin in the images are approximately $1320\,(\mathrm{W}) \times 1250\,(\mathrm{H})$ pixels. The images of the coins were captured with the lens aperture set to $f/5.6$ to achieve a good exposure while minimizing overexposure and maximizing depth of focus. They were converted from raw (NEF) files by the software utility DCRAW to linear 16-bit per channel (range: 0 to 65535) and stored as TIFF files.

The lightness of the images increases with increasing angle of elevation of the light source (Fig. 3). By digital processing (in MATLAB throughout this study), it is possible to make any weighted sum of the images, and hence to emulate the conventional photographic lighting configurations described above. For example, the image produced by the recommended axial illumination can be formed as the mean of the four images corresponding to the four lights nearest the camera, with elevation approximately 80 deg (last four images in the bottom row of Fig 3). The image produced by diffuse (i.e., omnidirectional) illumination is approximated as the mean of all 64 images. A weighted sum of the two, with 60% of the specular image plus 40% of the overall mean image, retains the shadowed outlines around the surface features, softened to reduce contrast (Fig. 4).

The outline of the coin is valuable as a feature to determine the scale and angle. Also, knowledge of the outline enables all subsequent image processing operations to be limited to the interior area, by using the outline as a pixel mask. The algorithm for constructing the outline, as illustrated in Fig. 5, was as follows:

Fig. 3 Montage of 64 images of the obverse of Faustina coin A, taken by a Nikon 200 camera in the UCL dome, illuminated by each of the 64 flash lights. The image brightness increases with angle of elevation of the light source, as shown from top of the figure (lowest angles) to the bottom (highest angles).

i. Compute the mean of the 16 images from Tier 4 and Tier 5 illumination.

ii. Extract the green channel and apply a 5×5 spatial median filter to the monochrome image.

iii. Compute the mean image intensities in outside region (corner) and inside region (center).

iv. Calculate intensity threshold as: $t = 0.5 \times (\text{meanoutside} + \text{meaninside} - 2 \times \text{stdevinside})$.

v. Plot one or more cross-sectional profiles. Check that the threshold level is above the background intensity and below the object intensity.

Fig. 4 (a) mean of images illuminated by top four flash lights; (b) mean of images illuminated by all 64 flash lights in dome; (c) weighted sum of the two, emulating the recommended photographic lighting configuration for coins.

vi. Make a binary mask at the same size as the original image, with 0 in the background (intensity < threshold) and 1 in the foreground (intensity > threshold).

vii. Convert binary mask to floating point and apply a 21×21 median filter to mask image to remove noise (i.e., spots in the object below threshold level).

viii. Apply a 3×3 smoothing filter to antialias the edge profile around outline mask.

ix. Convert floating point mask to an 8-bit grayscale image in range 0 to 255 and save as file.

x. Inspect the mask image and, if necessary, edit in Photoshop to tidy inside area.

xi. Determine coordinate points around the image outline by scanning all rows from both left and right and all columns from both top and bottom. Filter to remove duplicate points and sort into order of angle around circumference.

xii. Apply seven-point linear boxcar filter to smooth the coordinate points around the outline.

xiii. Compute centroid, mean and maximum radius, and length of perimeter.

Note that processing step (xi) allows, if necessary, for manual editing of the mask. Because the coin is photographed against a black background, the setting of the

intensity threshold in step (iv) ensures that the edge profile is well defined [Fig. 5(b)]. The interior area of the mask is completely clear if all of the image content is above the threshold. In practice, dark regions produced by shadowing of the surface relief may fall below the threshold and lead to unwanted intrusions within the mask interior [Fig. 5(c)]. These are easily removed by an erasure brush in Adobe Photoshop.

The area was calculated by two methods, first by treating the outline as an irregular polygon and triangulating each pair of points with the centroid,[31] and second by simply summing the number of pixels within the mask (Table 1). The eccentricity is the ratio of maximum to minimum radius from the centroid. All values were converted to mm using the image resolution of 75.3 pixels/mm.

2.2 *Coin Outlines from a 3-D Point Cloud*

The coins were digitized by a 3-D color laser scanner (Arius Technology Identik 300L), producing point clouds at a spatial resolution of 10×10 points/mm, i.e., a 0.1 mm GSD. Measurement uncertainty of the sensor is ± 0.035 mm in depth (z-axis) and of the order of ± 0.2 mm in the x- and y-axes due to planimetric point spacing and laser spot size. The technology is an optical recording technology combining spatial recording with color recording through the use of three laser wavelengths. The laser beam was orientated to scan the surface of the coins at an angle of 30-deg off normal, in order to reduce the effect of specular reflectance. The data were saved as a file in ".asc" format, in which each point is represented by one line of six numerical fields encoded as ASCII text. Table 2 shows the fields in the first five text lines, for five successive points along one vertical laser scan line.

It can be seen in Table 2 that the Y coordinate changed in successive points, as the laser beam was swept vertically, whereas the X coordinate remained almost constant. The 8-bit RGB signal values represent the reflected intensity at the three laser wavelengths of 638, 532, and 450 nm. In order to compare and combine the 2-D photographic image set with the 3-D point cloud, the latter was converted to a 2-D image with a pixel at each location in a 2-D image array with a resolution of 10×10 pixels/mm (grid spacing of 0.1 mm). The point cloud was "flattened" onto the Z plane, discarding the X, Y coordinates from the scanner, and taking the minimum of the R, G, B intensity values in each bin. For Coin A obverse, 89,226 points were mapped onto 23,524 pixels, a ratio of 3.79 points per pixel. The frequency distribution and resulting color image are shown in Fig. 6.

The mapping left some pixel locations in the grid unfilled, so a subsequent filling operation replaced each unfilled pixel by the mean of its nonzero neighbors (Fig. 7).

A DEM was computed from the 3-D point cloud by the same method, giving the height (in mm) at each location in the 2-D image array, taking the median of the multiple scanner Z coordinate values. The resulting DEM, after filling, is

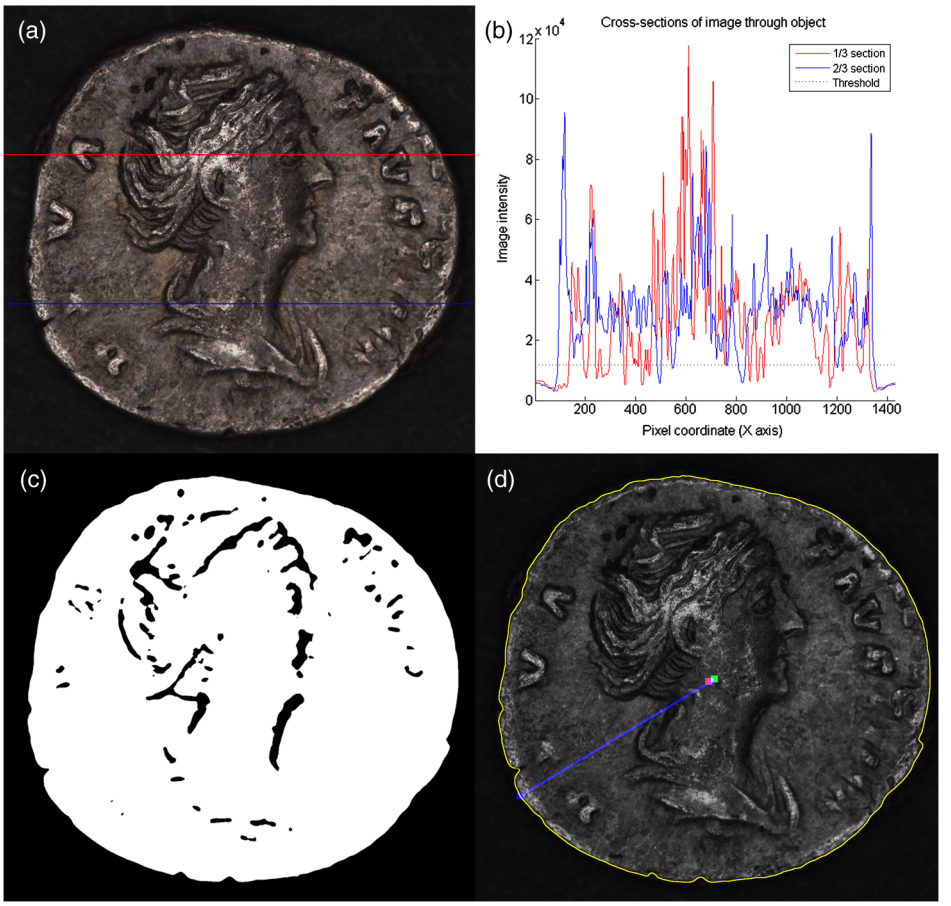

Fig. 5 Two cross-sections through image: (a) mean image with two cross-sections; (b) profiles of intensity of the green channel through cross-sections with threshold; (c) binary mask before editing; and (d) monochrome image showing outline, centroid and vector of maximum radius.

Table 1 Dimensions of Faustina coins (mm) from computation of outline.

	Coin A obverse	Coin A reverse	Coin B obverse	Coin B reverse
Perimeter length	49.26	50.54	48.13	47.88
Area in mm^2 (polygon method)	226.5	233.4	216.0	213.7
Area in mm^2 (mask method)	227.3	234.2	216.8	214.5
Mean radius	8.49	8.62	8.30	8.25
Eccentricity	1.134	1.187	1.100	1.093

Table 2 First five lines from the .asc file for coin A obverse.

X	*Y*	*Z*	*R*	*G*	*B*
−404.830994	−273.773987	−123.266998	162	194	147
−404.829010	−273.610992	−123.323997	184	223	159
−404.828003	−273.596985	−123.254997	136	161	126
−404.826996	−273.532013	−123.261002	134	160	128
−404.826996	−273.500000	−123.219002	149	178	138

shown in Fig. 8 as a monochrome image (a), scaled from black (minimum) to white (maximum), and as a 3-D terrain plot (b).

The outline of the image from the flattened point cloud was computed from the RGB image in the same way as for the photographic images, as described in Sec. 2.1. Because the spatial resolution is much lower, the scanner outline has much less detail (Fig. 9) and the line of maximum radius occurs at a different angle (compare Fig. 5).

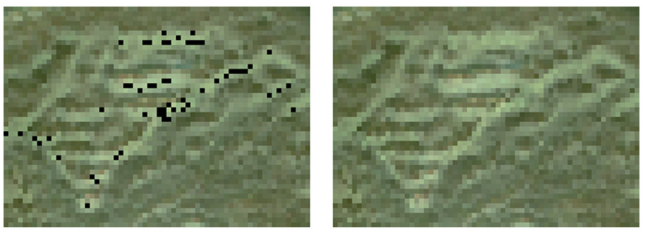

(a) (b)

Fig. 7 (a) Detail of Faustina's hair, showing pixels unfilled after mapping and (b) after filling.

2.3 *Scaling and Registration of Images*

The photographic images from the camera in the dome and the pseudoimage generated by flattening the 3-D point cloud are of very different sizes and at slightly different orientations. An efficient way is needed to determine both scale factor and rotation angle to bring them into alignment. Although this could be done on the 2-D images by a search-and-correlate algorithm, such as SIFT, the method preferred in this study uses the two outlines. Their irregularity is sufficient to provide a characteristic signature that facilitates the transformation.

Normalizing the radius of each point relative to the mean radius and plotting against angle gives the graphs of Fig. 10(a), showing $r(\theta)$ versus θ. Although the radius varies by less than $\pm 7\%$, a similar pattern can be seen for both outlines. The number of points around the outline is a measure of the circumference of the shape, hence the ratio of their lengths gives the relative linear scale factor, in this case, $3709/493 = 7.523$.

By scaling the two outlines to equal length, then interpolating each to units of 0.01 deg (i.e., a vector of 36,000 values) and sliding one vector along the other, the position of best fit can be found. To avoid wraparound at 360 deg, the reference outline is duplicated so that its vector of 72,000 points represents two full revolutions 0 to 720 deg. Determination of the goodness-of-fit is achieved by cross-correlation between the two 36,000-element vectors, one fixed (the reference outline from the scanner) and the other extracted at successive positions from the duplicated image outline. The maximum value of the coefficient of correlation indicates the angle of best fit

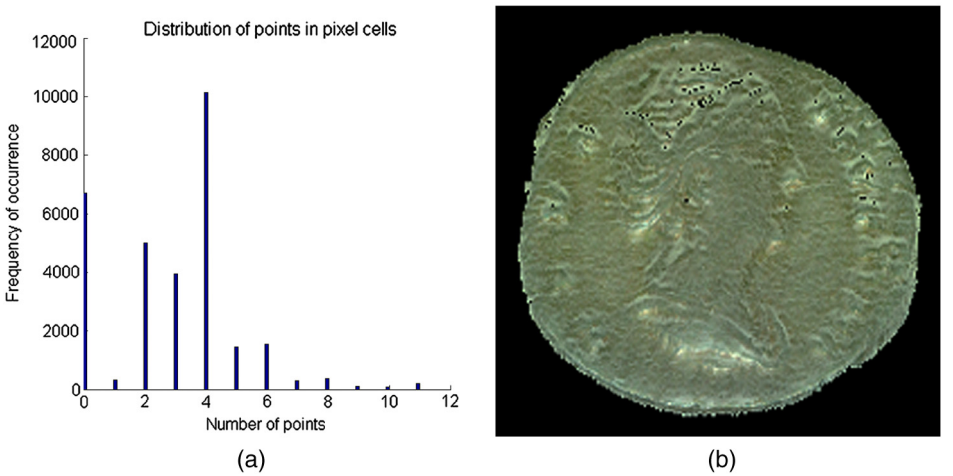

(a) (b)

Fig. 6 (a) Distribution of number of points mapped onto each pixel and (b) resulting RGB image.

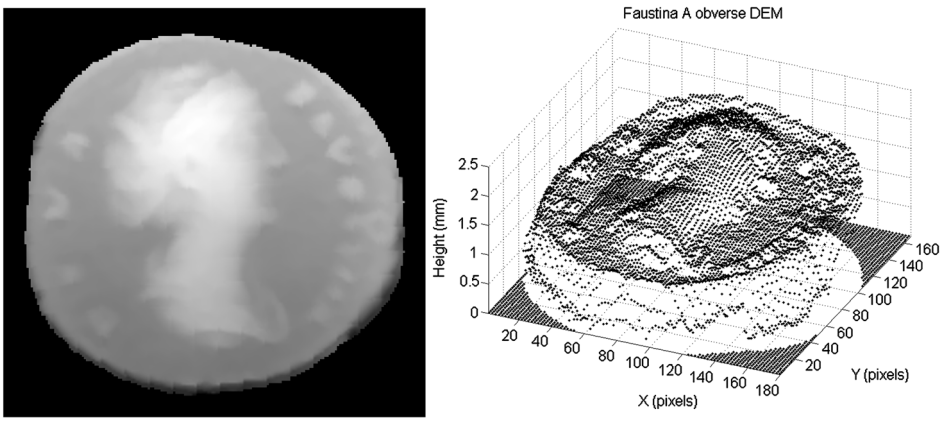

Fig. 8 Digital elevation map from scanner, represented as (a) monochrome image and (b) 3-D surface plot.

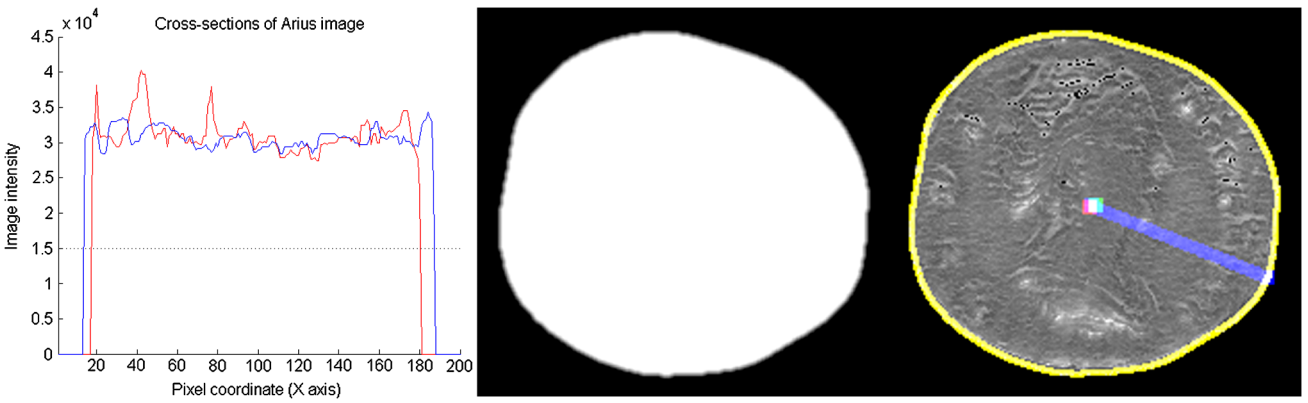

Fig. 9 Flattened image from scanner: (a) Intensity profiles; (b) outline mask; and (c) outline, centroid, and vector of maximum radius.

[Fig. 10(b)], with the peak at 354.83 deg. Note that the second positive peak at 170.59 deg is almost diametrically opposite, indicating a slightly elliptical outline shape.

By the above method of outline correlation, both the scaling factor κ and rotation angle θ can be found to map one outline onto the other. In this case, the scaling factor is 7.523 and the rotation angle is 5.17 deg (anticlockwise). This provides a means for every point in the reference images for the DEM (i.e,. height map), derived from the scanner point cloud, to be transformed by a 2×2 matrix into close registration with a corresponding point in images from the camera:

$$\begin{bmatrix} x_t \\ y_t \end{bmatrix} = \mathbf{M} \begin{bmatrix} x_r \\ y_r \end{bmatrix},$$

$$\text{where } \mathbf{M} = \kappa \begin{bmatrix} \text{cosd}(\theta) & \text{sind}(\theta) \\ -\text{sind}(\theta) & \text{cosd}(\theta) \end{bmatrix} = \begin{bmatrix} 7.4084 & -0.6703 \\ 0.6703 & 7.4084 \end{bmatrix}. \quad (1)$$

The result of the transformation is shown in Fig. 11(a), in which the original scanner outline is colored in red, the scaled scanner outline in green, and the photo outline in blue. In Fig. 11(b), there is a two-color composite image with the enlarged and rotated height map from the scanner in the red channel and the Z component of the photometric normals (see Sec. 2.4) in the green channel.

2.4 *Calculation of Photometric Normals*

Photometric normals were calculated from the photographic image sets taken under directional lighting in the dome, using the "shape from shading" principle. The difficulty with silver and other metals, and indeed with all shiny and glossy materials, is that they reflect strongly in the specular direction. So, in the vector of 64 intensity values for any pixel, there are a few values much larger than the others, corresponding to positions where the surface normal is close to the bisector of the angle between the illumination vector (toward the light) and the view vector (toward the camera). This results in images with high dynamic range, where a few pixels may be 10 times greater in value than the majority. The two coins in this study have been cleaned, and so are reasonably bright, but they do not have the mirror-like quality of newly minted coins. Close examination shows signs of wear, pitting, scratches, corrosion, and tarnishing of their surface,

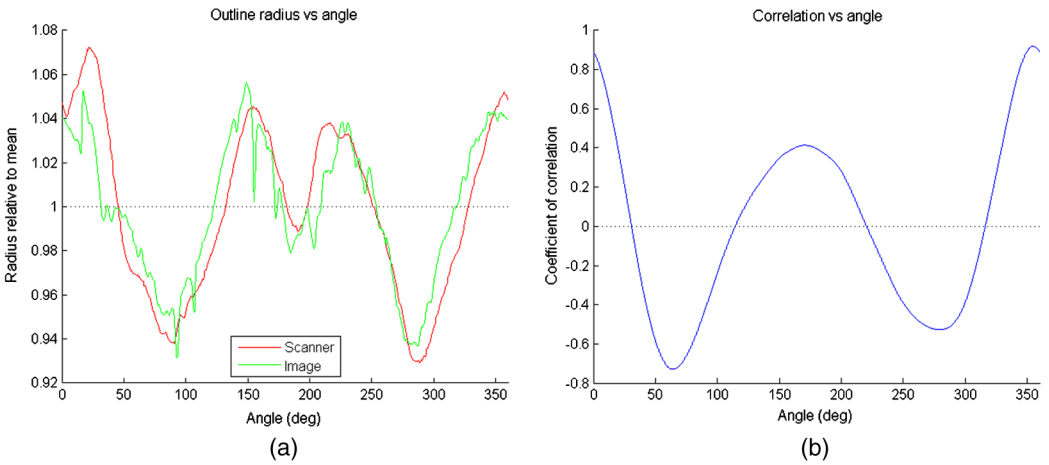

Fig. 10 (a) Normalized outline radius versus angle and (b) outline correlation coefficient versus angle.

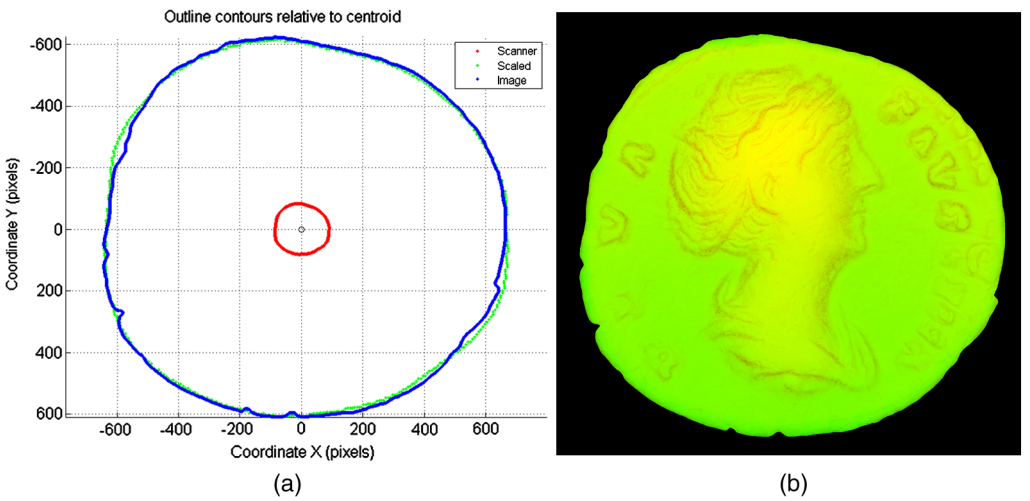

Fig. 11 (a) Superimposed outlines after scaling and rotation and (b) composite image of scanner height (red) and photometric normals (green).

all of which contribute to the patina and cause some scattering of the reflected rays and diminution of their intensity.

Figure 12 shows the intensity distribution for a single pixel on the tip of Faustina's nose in coin A obverse. There are three peaks, where the pixel intensities reach values in the range 3000 to 4500 but most others are <500. The magenta curve shows what the intensities would be for a perfectly matte (Lambertian) surface with the same albedo and normal angle. It is clear that the specular peaks are much greater in intensity than for the cosine, but for other angles, the distributions are similar.

The surface normals were calculated, therefore, by using a subset of the intensity distribution, as shown in blue in Fig. 12(b), corresponding to angles of incidence, where the reflected intensity is similar to that of an equivalent matte surface. This is dubbed the "bounded regression" technique.[32] The resulting normals are shown in conventional false color in Fig. 13(a).

Following the rotation and scaling of the DEM from the scanner, a further operation was required to ensure that it was spatially aligned as well as possible with the photometric normals [Fig. 11(a)]. Image cross-correlation was used by cropping a section near the center of the photometric normals and sliding it around within the scaled DEM until the best match was achieved. This was performed on both X and Y gradient images and the results combined. The gradients p and q are defined as the partial derivatives of the surface height with respect to the two axes x and y:

$$p = \frac{\partial z}{\partial x}, \qquad q = \frac{\partial z}{\partial y}. \tag{2}$$

Gradients were derived from the scanner DEM directly by taking first-order differences along rows and columns. Gradients were derived from the photometric normals by taking ratios of their components and as shown in Figs. 13(b) and (c):

$$p = \frac{N_x}{N_z}, \qquad q = \frac{N_y}{N_z}. \tag{3}$$

The displacement between the photometric image and the transformed scanner image was determined by cross-correlation between the surrounding regions of the image gradients. One

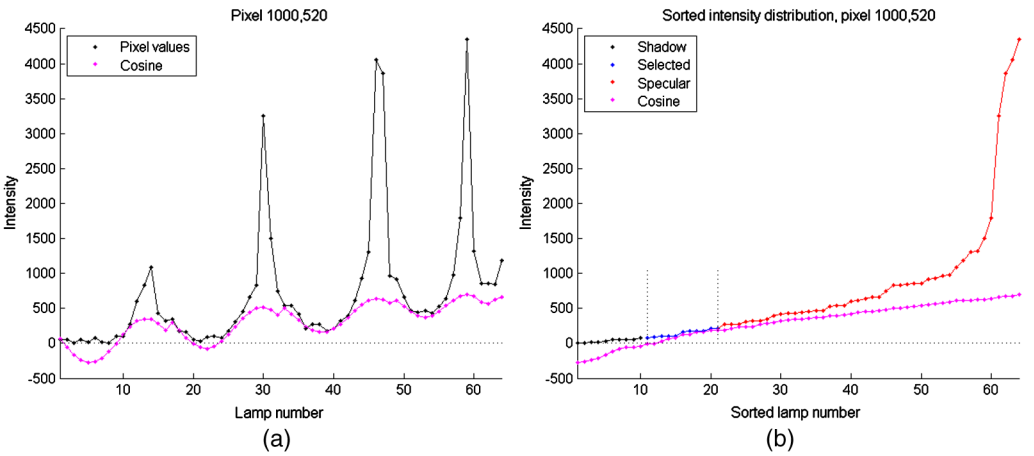

Fig. 12 Intensity distributions for a single pixel in coin A: (a) in lamp order and (b) sorted.

Fig. 13 (a) Photometric normals; (b) X gradients; and (c) Y gradients.

section of the gradient image A (test) was taken as a template and correlated with a corresponding section of the gradient image B (reference), using the MATLAB function `corr2` to calculate the correlation coefficient r:

$$r = \frac{\sum_m \sum_n (A_{mn} - \bar{A})(B_{mn} - \bar{B})}{\sqrt{\left[\sum_m \sum_n (A_{mn} - \bar{A})^2\right]\left[\sum_m \sum_n (B_{mn} - \bar{B})^2\right]}}. \quad (4)$$

This equation has the advantage of being independent of the brightness and contrast of the template A and image B, because it takes differences from their respective means and normalizes the intensity values of both. A section of 201×201 pixels from the test gradient image was moved over the fixed reference gradient image with successive pixel displacements in both axes, and at each position the correlation coefficient was calculated. The resulting array of 201×201 values in the range $[-1, +1]$ can be visualized as a surface on which the maximum value represents the position of best fit (Fig. 14). The different correlation surfaces arising from the X and Y gradients [Figs. 14(a) and 14(b)] are combined by taking the pixelwise product of the correlation scores [Fig. 14(c)]. Note that the figure shows an image region of 301×301 pixels, which is unrelated to the kernel size of 201×201 pixels.

The effectiveness of taking the product of the separate correlation scores for X and Y gradients can be seen by viewing the score as a 3-D surface [Fig. 15(a)]. The peak of the combined distribution is localized and very clearly defined. Using these X, Y offset values to translate the photometric normals relative to the scanner DEM gives the optimum registration of the two images [Fig. 15(b)]. The blue channel

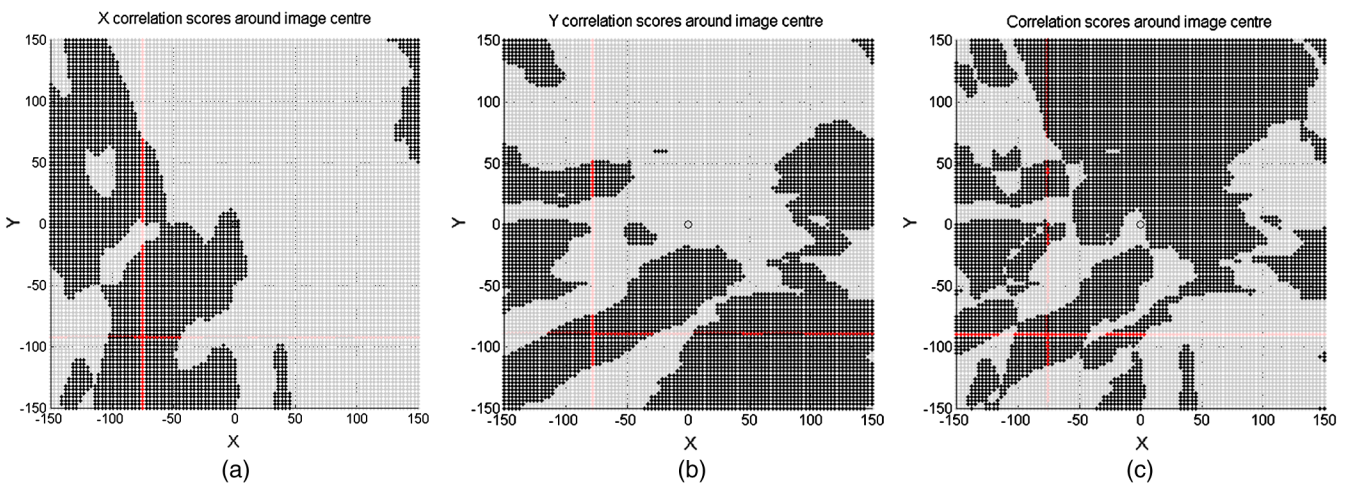

Fig. 14 Correlation scores with maxima (red lines) for (a) X gradients; (b) Y gradients; and (c) product. Positive values are indicated by black points, whereas negative values are indicated by gray points. The red lines cross at the pixel of maximum value.

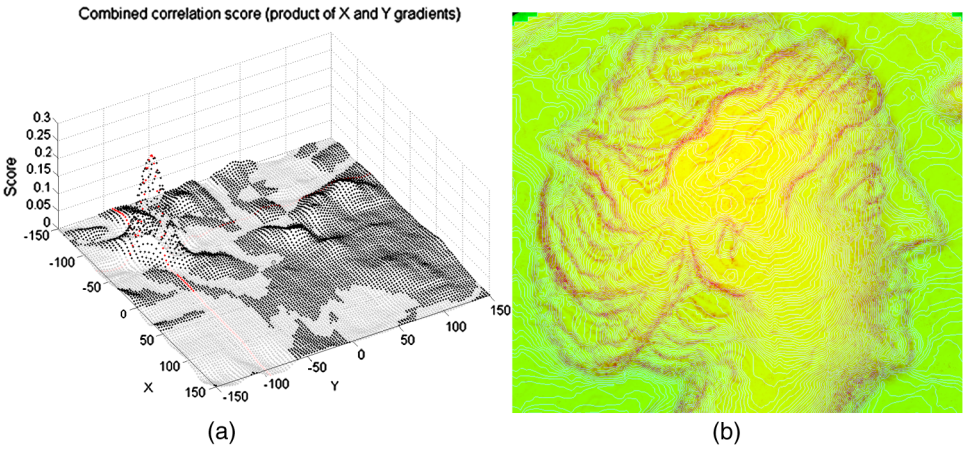

Fig. 15 (a) Combined correlation scores plotted as a surface in 3-D view and (b) registered image detail.

in this image has been filled with a dense edge pattern produced by applying a Sobel edge detection filter to the scanner DEM image. This adds a pleasing texture for visualization.

2.5 *Combining Low and High Spatial Frequencies*

Having registered the two representations, the final step was to combine them into a single DEM to obtain the geometric accuracy of the laser scanner with the fine spatial detail and accurate color of the camera. It was previously shown how this could be achieved for a small number of manual height measurements at selected points on a surface.[31] The method relies on an algorithm by Frankot and Chellappa,[33] who observed that, when integrating the surface gradients, if additional low-frequency information could be obtained from another source, then the accuracy of the surface reconstruction could be enhanced. A related study demonstrated the viability of combining low and high frequencies in the Fourier domain.[34] In the present study, we sought to show that the method could be extended to make use of the low frequency height data from the laser scanner.

The DEM from the scanner was heavily filtered, first by a 5×5 median filter to remove isolated noise, then by an 11×11 box averaging filter to remove spatial variations of scale finer than about 1 mm. Taking the 2-D Fourier transform of the resulting smoothed DEM gives the spatial $\log_{10}(\text{power})$ distribution in Fig. 16(a). Almost all of the power is concentrated in a small region at the center of the shifted frequency plane, apart from a few slanted lines across the plane at higher frequencies caused by the sampling grid pattern.

Applying the Frankot–Chellappa transform to integrate the photometric gradients provides the high spatial frequencies of the surface. Plotting the $\log_{10}(\text{power})$ distribution in false color in the shifted frequency plane [Fig. 16(b)] shows a concentration of power at all phases, extending out to approximately one half of the diameter of the plane. Scatterplotting the values as one-dimensional distributions along the X axis from the center gives the graphs of Fig. 17(a), showing that the photometric data has a power about 2 log units (i.e., a factor of 100×) greater than the scanner data.

The two frequency distributions were combined by a linear interpolation ("lerp") function of radius from the center of the shifted frequency plane [curves at the base of Fig. 17(a)]. The low frequencies were taken from the scanner and the high frequencies from the camera:

$$P(\omega) = \alpha(r)\mathrm{LF}(r) + (p_L/p_H)[1 - \alpha(r)]\mathrm{HF}(r). \quad (5)$$

The gain factor is needed to balance the contribution of each frequency band and is the ratio of the summed power of each distribution in a narrow band spanning the crossover frequency. The blending function in the intermediate

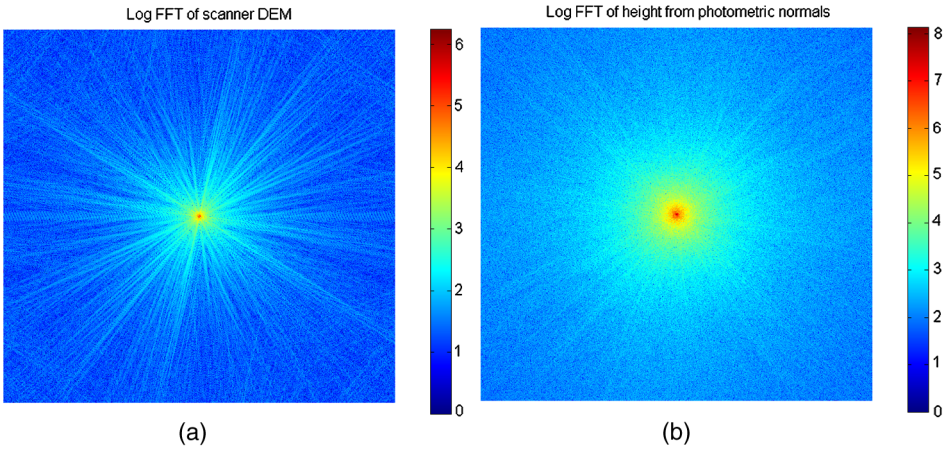

Fig. 16 $\text{Log}_{10}(\text{power})$ distributions in Fourier spatial frequency domain: (a) scanner and (b) photometric.

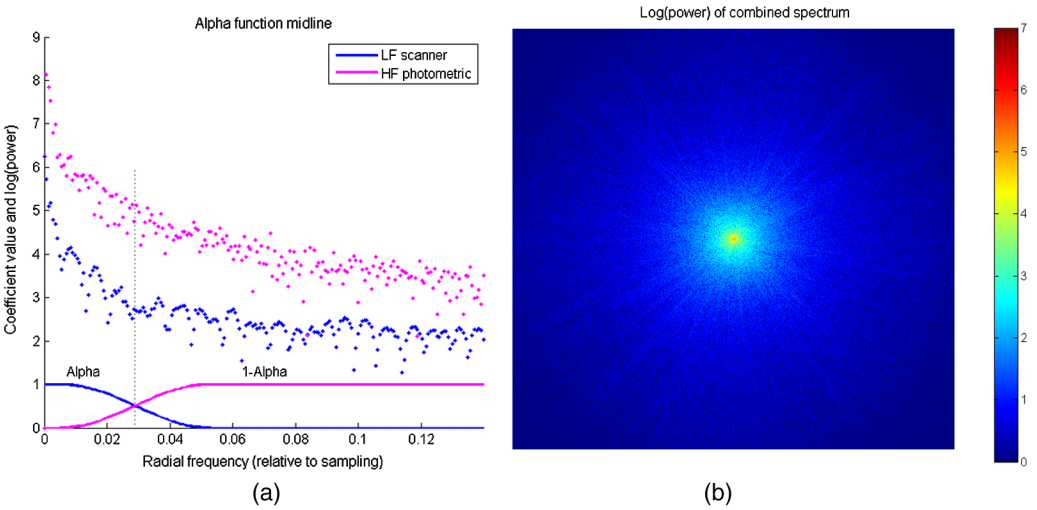

Fig. 17 (a) $\mathrm{Log}_{10}(\mathrm{power})$ cross-sections and merging function and (b) merged distribution.

(cross-over) frequency region is constructed from a modified Hann function:

$$\alpha(r) = [1 + \cos(\pi r')]/2, \tag{6}$$

where $r' = (r - r_{\min})/(r_{\max} - r_{\min})$ for $r_{\min} \le r \le r_{\max}$.

The limits of the cross-over region were set to $r_{\max} = 75$ and $r_{\max} = /10$. Note that the image width is 1430 pixels, so the Nyquist limit in the Fourier domain is 715 pixels. The horizontal axis of Fig. 17(a) is scaled relative to the sampling frequency, so the Nyquist value would be 0.5 The combined log(power) distribution is shown in Fig. 17(b).

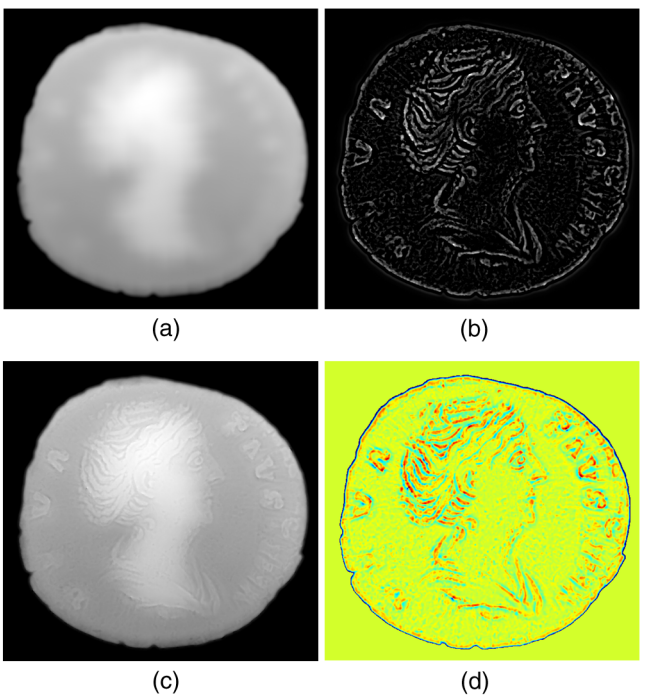

Fig. 18 Spatial frequency components: (a) low frequencies from scanner; (b) high frequencies from camera; (c) combined; and (d) difference map.

The effect of the blending function in determining the contribution of low spatial frequencies from the scanner and high spatial frequencies from the camera can be seen in the images of Fig. 18, which are scaled so that white is highest and black is lowest. The image at Fig. 18(a) is produced from the inverse Fourier transform of $\alpha(r)\mathrm{LF}(r)$ and the image at Fig. 18(b) is produced from $[1 - \alpha(r)]\mathrm{HF}(r)$. The combined image [Fig. 18(c)] shows the full range of spatial frequencies. The color-coded difference map shows the difference between the reconstruction and the original DEM from the scanner, which corresponds closely to the high frequency components from the camera.

The reconstructed surface shown as an image in Fig. 18(c) is plotted as a 3-D view in Fig. 19. The form slopes downward in the Y direction, because the coin lay on a sloping support under the laser scanner.

A horizontal cross-section (Fig. 20) shows the close correspondence between the scanner DEM and the reconstructed surface. The height everywhere is very close, but the reconstructed surface has much more detail. The local detail is particularly evident where the section passes (left to right) through the contours of the braided hair, the helix and antihelix of the ear, the ala above the nostril, the tip of the nose, and the side arm of the letter U. Particularly in the region across the ear, the greater depths of penetration behind the helix and into the supratragic incisure are both apparent.

For improved rendering, a pseudo-albedo of the coin was constructed as the mean of all 64 images, minus one third of the Tier 5 lamps (numbers 61 to 64) to reduce the frontal specularity. The R, G, B values for each pixel were written, together with the X, Y, Z coordinates and normal components Nx, Ny, Nz to a file in asc format, with nine values per line for each point inside the outline. The total number of lines in the file (i.e., points in the DEM) was 1,288,556, an increase by a factor of 14.4 over the number in the original laser point cloud. The resulting file produces a beautiful rendering of the coin when viewed in "CloudCompare" software (Fig. 21). The effect on the final composite height map is to enhance both the fine detail and the edge contrast of the lettering, the hair, and the profile of the face.

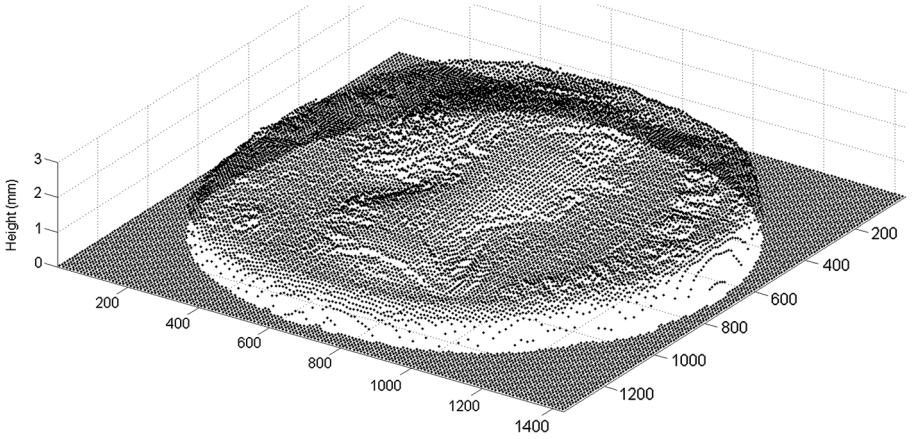

Fig. 19 Reconstructed 3-D surface from combined Fourier power spectrum (plotting every 10th pixel).

3 Analysis and Evaluation of Obtained Digital Elevation Map and Other Datasets of Coins

3.1 *Overview and Description of the Datasets*

The geometric quality of the DEM derived by the method described above was evaluated by comparison with three other models. The 3-D datasets for the two coins were acquired by different institutions in the COSCH network, using distinct systems, methods, and procedures. Figure 22 shows the general workflow, where the final outcome and overall accuracy of the model depend intrinsically on all the previous steps. Moreover, these coins were captured at different times over a 2-year period: before and after they had been subjected to ultrasonic cleaning with isopropanol and/or coating by Helling 3-D scanning spray (Helling GmbH) of titanium oxide (TiO_2), using an airbrush with compressor. In the cases where the 3-D acquisition was done with the coating, the powder was subsequently cleaned mechanically and any remaining powder was removed with distilled water and surface dried with hot air. These procedures, along with handling and metal oxidation, certainly caused variations in the specularity of the coin surfaces, and may likely have changed the fine geometry of the 3-D models.

Although all measurements are subject to error, when planning the 3-D data acquisition and processing strategy, it is fundamental to consider sources of measurement error and the uncertainty of measurement results.[35–39] These are not only characteristics of the hardware and software but may also arise from the nature of the object, the environment, and human factors (Fig. 23).

Table 3 presents a short description of the dataset used for comparison, though it does not represent the possible highest quality outcome of the systems and techniques that were used (as the aim of the case study had not been yet formulated at the time of acquisition of some of the 3-D data). A more comprehensive description of the 3-D data

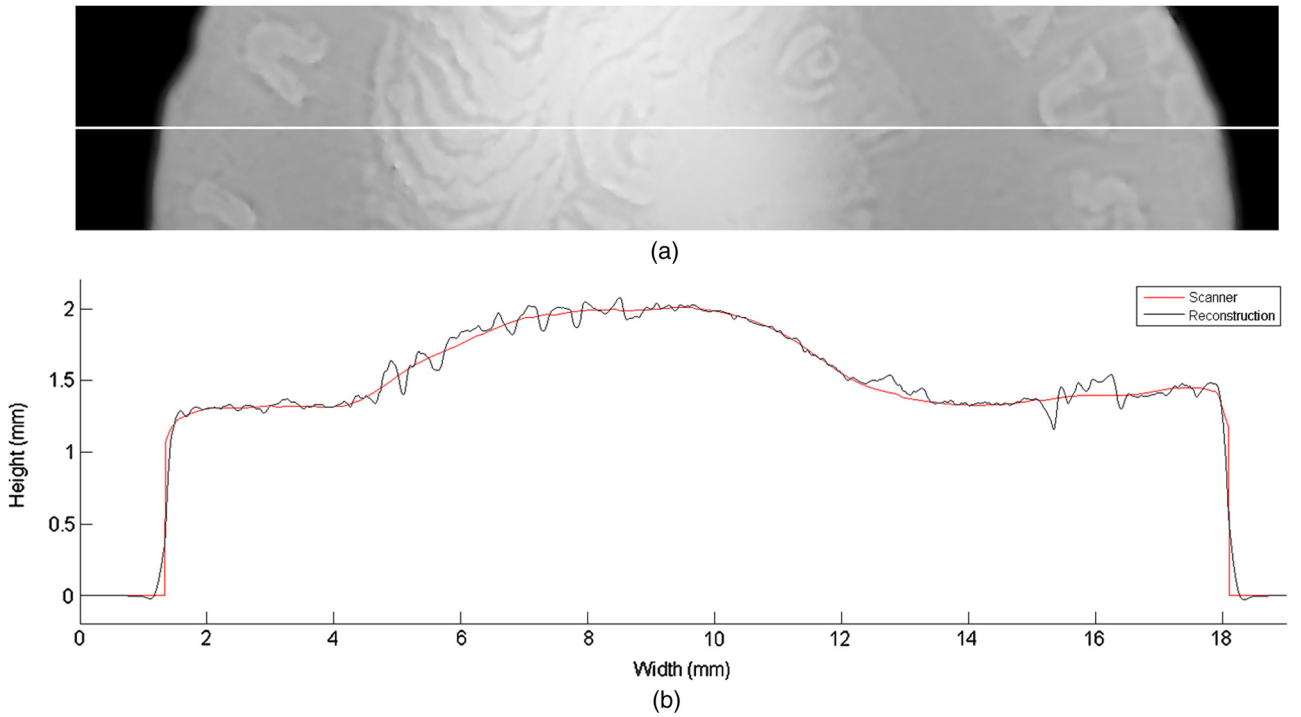

Fig. 20 Horizontal section with elevation showing (a) scanner height and (b) reconstruction.

Fig. 21 Final reconstruction of Faustina A obverse, viewed in "CloudCompare."

acquisition process and postprocessing of the data, including metadata and paradata, can be found in the case study's record template.[40]

The features to be captured in the coins should not be smaller than the GSD, i.e., the finest resolution of the digitizing system. The SmartSCAN records of the coins were taken at 20-μm sampling distance, meaning that the smallest feature expected to be identified should be 40 μm. Different resolutions may reveal, distort, or conceal topographical details of the surface. This issue is of great importance when analyzing and interpreting physical characteristics of the coins, e.g., variations in the hammering process, die, mint signs, scratches, wear pattern of the used stamp, or cut and punchmarks.[14]

A few basic geometrical and topological measurements of the complete 3-D models—i.e., obverse and reverse aligned and merged into one single model—were computed with Geomagic Control 2015.1.0 (3-D Systems) and Polyworks IMEdit and IMInspect 2015 IR12 (Innovmetric) software and are shown in Table 4.

"As the appearance of an ancient coin is often unique (...), the shape of the coin edge is regarded to be an important feature to characterize a coin."[19] Shape factor, sometimes called "circularity," is a compact measure of shape, which can be used to quantify the degree to which an object resembles a circle. The shape factor of a circle is 1, and by the isoperimetric inequality, any object which is not a circle will have a value <1. Shape descriptors must be invariant to scaling and Euclidean transformations. This one is similar to roundness, yet emphasizes the configuration of the perimeter by reflecting the smoothness of contour, rather than the length relative to object area.[21] Shape factor is defined as:

$$\text{Shape factor} = \frac{4\pi A}{p^2}, \tag{7}$$

where A is a measure of the surface area of the object, taken from the cross-section in the XY plane of each coin, and p is the perimeter of the contour.

Volume and weight are "relevant to calculate the density of the coin to identify differences between the theoretical and the real density when coins were plated (for instance, a silver over a copper core)."[14] The coins were weighted at RBINS, using a Sartorius B120S: coin A weighed 3.0939 g, whereas coin B weighed 2.8486 g. Density (ρ) is expressed here in g/cm^3 and defined by Eq. (8):

$$\rho = m/V, \tag{8}$$

where m is the mass and V is the volume.

The 3-D complete model acquired with Mechscan has the highest number of vertices and polygonal faces, potentially showing finer details (i.e., should none of the 3-D point clouds or meshes have been decimated or subdivided, and excluding computational artifacts), whereas the models acquired by SfM have the lowest number of vertices and polygonal faces, potentially showing fewer details—these characteristics may also help explaining the differences in the final size and other measurements of the coins. For maximum diameter, the SmartSCAN and Mechscan yielded identical values (18 mm) for coin A, with SfM measuring 0.2 mm less; all yielded different values in the range of 17.54 to 18 mm. For surface area, the highest values were from Mechscan and the lowest from SfM. Mechscan gave the largest volume for coin A, while SmartSCAN had the larger volume for coin B, whereas SfM presented the smallest volume for both coins. For shape factor, the SmartSCAN and SfM yielded identical values (0.96) for coin A, with Mechscan indicating a lower circularity (0.92); whereas for coin B, all presented similar values (between 0.97 and 0.99). This result also indicates that coin B resembles a circle more than coin A. Concerning density, because the SfM models present

Fig. 22 3-D acquisition workflow: from choosing a 3-D data acquisition system to generating a 3-D digital model.[21]

Fig. 23 Sources of measurement error that lead to uncertainty of measurement results.[21]

Table 3 Short description of the 3-D dataset available for comparison.

Coin	3-D model	Survey institution	3-D data acquisition system type	3-D data acquisition system model	Acquisition resolution[a]
A,B	SmartSCAN HE	AICON 3-D Systems	SLS	SmartSCAN HE with 8MP color stereo cameras, FOV 75	20 μm (XY) 3 μm (Z)
	Mechscan	Royal Belgian Museum of Natural Sciences (RBINS)	SLS	Mechscan 3-D Macro Scanner	11 μm (XY)
	DEM	University College, London (UCL)	Color Laser Scanner combined with Photometric Imaging	IDENTIK 300L, AriusTechnology Scanner; Nikon D200, Nikkor 200 mm Macro Lens, $f/5.6$	13 μm (XY)
	SfM	Royal Belgian Museum of Natural Sciences (RBINS)	SfM	Canon 600D, Canon Macro Lens EF 100 mm 1:2.8, $f/8$	n.a.

[a]Lateral resolution value for the lateral dimensions (X and Y) in the center of the measuring volume, according to the manufacturer.

the lowest volume values, it is not surprising that their density is higher. However, one should be cautious when interpreting density as this was determined here by measuring the total mass and the total volume of the 3-D digital surface models of each coin, and these coins are made of different materials (i.e., silver alloy). A more comprehensive description about the elemental composition can be found in Ref. 41.

3.2 *Pairwise Best Fit Alignment*

Because the accuracy of a complete 3-D model of each coin is also directly dependent on the alignment and merging of its obverse and reverse, we decided to analyze these separately. Geomagic software was used to align the pairwise 3-D models. SmartSCAN HE, Mechscan, and SfM were set as reference models, and the DEM was set as test model. The following steps were used as a standard procedure for all 3-D models: (a) feature-based alignment, using $\geq$3 points, for a first rapid alignment; (b) best-fit alignment, with parameters: sample size 100,000 (maximum allowed), tolerance 0.01 mm, high-precision fitting, and automatic deviator elimination. The results of pairwise best-fit alignment are presented in Tables 5 and 6.

Geomagic software was also used for pairwise comparison between 3-D models, with the following parameters: maximum deviation: 0.1 mm; critical angle: 45 deg; max. critical: 0.1000; max. nominal: 0.0100; min. nominal: −0.0100; and min. critical: −0.1000. Again, SmartSCAN HE, Mechscan, and SfM were set as reference, and DEM was set as test. The results of the pairwise comparison (average deviation, standard deviation, and deviation distribution of points) are presented in Tables 5 and 6, as well as in Figs. 24–26.

Comparison between the 3-D reference models and the DEM test model of Coin A shows that on the reverse face, the alignment of the pairwise models gave the same RMS values (0.05 mm) and average error (0.04 mm). The maximum deviation was in the range of $\pm$0.1 mm, with an average deviation of $\pm$0.03 mm and a standard deviation of 0.04 mm. The deviation distribution of points indicates that SmartSCAN and Mechscan present greater similarities with the DEM, though only some 22.8% of points lie in the range of $\pm$0.01 and near to 50% lie in the range of $\pm$0.025 mm. The areas of highest deviation are concentrated around the figure of Aeternitas, as well as along the perimeter and upper part of the coin (Fig. 24).

For the obverse of coin A, the alignment of the pairwise models indicates the same average error (0.04 mm). The RMS error for SmartSCAN is 0.07 mm, 0.01 mm higher

Table 4 Topological, geometrical, and density measurements of the complete 3-D models (i.e., obverse and reverse aligned and merged into one single model).

Coin	Software	Vertices (points)	Triangles (faces)	Max. diameter (mm)	Surface area (mm^2)	Volume (mm^3)	Shape factor	Density (g/cm^3)
A	SmartSCAN HE	54,0191	108,0380	18	540.67	320.26	0.96	9.2
	Mechscan	13,42685	2,685,266	18	549.13	325.39	0.92	9.51
	SfM	20,0002	400,000	17.8	525.42	318.6	0.96	9.71
B	SmartSCAN HE	55,8419	111,6834	18	535.08	344.62	0.99	8.13
	Mechscan	12,62963	252,5663	17.74	539.28	342.35	0.97	8.33
	SfM	42,1118	842,232	17.54	514.93	337.5	0.98	8.44

Table 5 Coin A: pairwise alignment (RMS error and average error) and 3-D general comparison (average deviation, standard deviation, deviation distribution of points between ±0.01 and ±0.025 mm).

		Alignment		3-D general comparison			
Coin A	3-D model (reference)	RMS error (mm)	Average error (mm)	Average deviation	Standard deviation	Deviation distribution ±0.01 mm(%)	Deviation distribution ±0.025 mm (%)
Reverse	SmartSCAN HE	0.05	0.04	0.03/ – 0.03	0.04	22.77	49.53
	Mechscan	0.05	0.04	0.03/ – 0.03	0.04	22.75	49.77
	SfM	0.05	0.04	0.03/ – 0.03	0.04	21.69	48.78
Obverse	SmartSCAN HE	0.07	0.04	0.03/ – 0.03	0.03	23.48	55.28
	Mechscan	0.06	0.04	0.03/ – 0.03	0.03	25.32	58.29
	SfM	0.06	0.04	0.03/ – 0.03	0.03	26.5	58.67

Table 6 Coin B: pairwise alignment (RMS error and average error) and 3-D general comparison (average deviation, standard deviation, deviation distribution of points between ±0.01 and ±0.025 mm).

		Alignment		3-D general comparison			
Coin B	3-D model (reference)	RMS error (mm)	Average error (mm)	Average deviation	Standard deviation	Deviation distribution ±0.01 mm (%)	Deviation distribution ±0.025 mm(%)
Reverse	SmartSCAN HE[a]	0.08	0.06	0.04/ – 0.04	0.05	15.95	38.46
	Mechscan[a]	0.08	0.06	0.04/ – 0.04	0.04	16.17	38.99
	SfM[a]	0.08	0.06	0.04/ – 0.04	0.05	15.91	38.41
Obverse	SmartSCAN HE	0.07	0.05	0.03/ – 0.03	0.04	19.98	46.85
	Mechscan	0.07	0.04	0.03/ – 0.03	0.04	19.92	46.97
	SfM	0.06	0.04	0.03/ – 0.03	0.04	21.5	50.51

[a]Note that 13%, 12%, and 14% of the DEM points were too far away from the SmartSCAN, Mechscan, and SfM models, respectively, to be used in the computation.

than for Mechscan and SfM (0.06 mm). The maximum deviation is in the range ±0.1 mm, with an average deviation of ±0.03 and a standard deviation of 0.04. The deviation distribution of points indicates that SfM (followed by Mechscan and SmartSCAN) presents higher similarities with the DEM, with 26.5% of points lying in the range of ±0.01 and 58.3% lying in the range of ±0.025 mm. Areas of highest deviation are mostly concentrated in areas with higher topographical differences, such as along the letters and most of the bust of Faustina.

For the reverse of coin B, the alignment of the pairwise models indicates the highest RMS (0.08 mm) and average error (0.06 mm) of all cases. About 13% of the DEM points were too far away from the SmartSCAN model, 12% from the Mechscan model, and 14% from the SfM model, and were excluded from the computation. The average deviation was ±0.04 mm and standard deviation was between 0.04 and 0.05 mm. The deviation distribution of points indicates very similar results, though with only a small number of points lying in the range of ±0.01 mm and <40% lying in the range of ±0.025 mm. Areas of highest deviation are again concentrated on the figure, as well as along the perimeter and upper part of the coin (Fig. 25).

For the obverse of coin B, the alignment of the pairwise models indicates an RMS error between 0.06 and 0.07 mm, and an average error between 0.04 and 0.05 mm. The average deviation is ±0.03 mm and standard deviation is 0.04 mm. The deviation distribution of points indicates that SfM presents higher similarities with the DEM, with 21.5% of the points lying in the range of ±0.01 mm and 50.5% lying in the range of ±0.025 mm. Areas of highest deviation are once again concentrated in areas with higher topographical differences.

Several cross-sections on the *XZ* and *YZ* planes were also generated, in order to facilitate detailed analysis on the morphology of the profiles (Fig. 27).

4 Discussion of Results

As expected, different systems, software, and parameters may yield 3-D models with different topological and

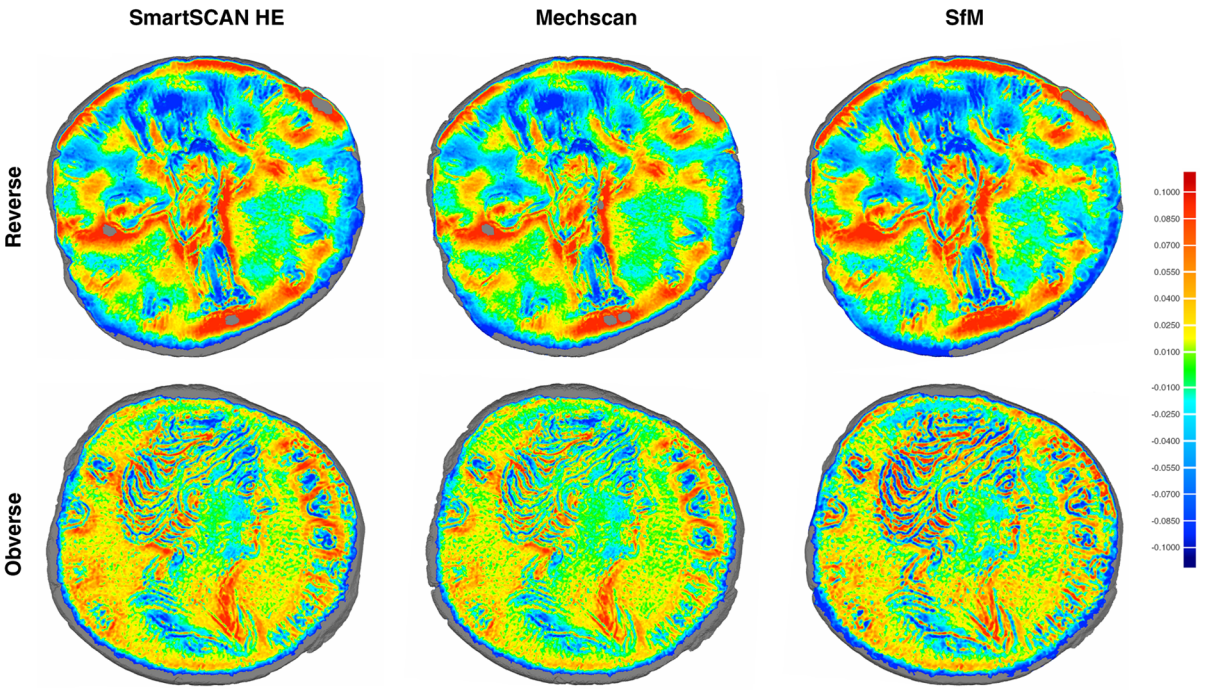

Fig. 24 Color deviation maps from pairwise comparison of DEM with 3-D models of obverse and reverse of coin A.

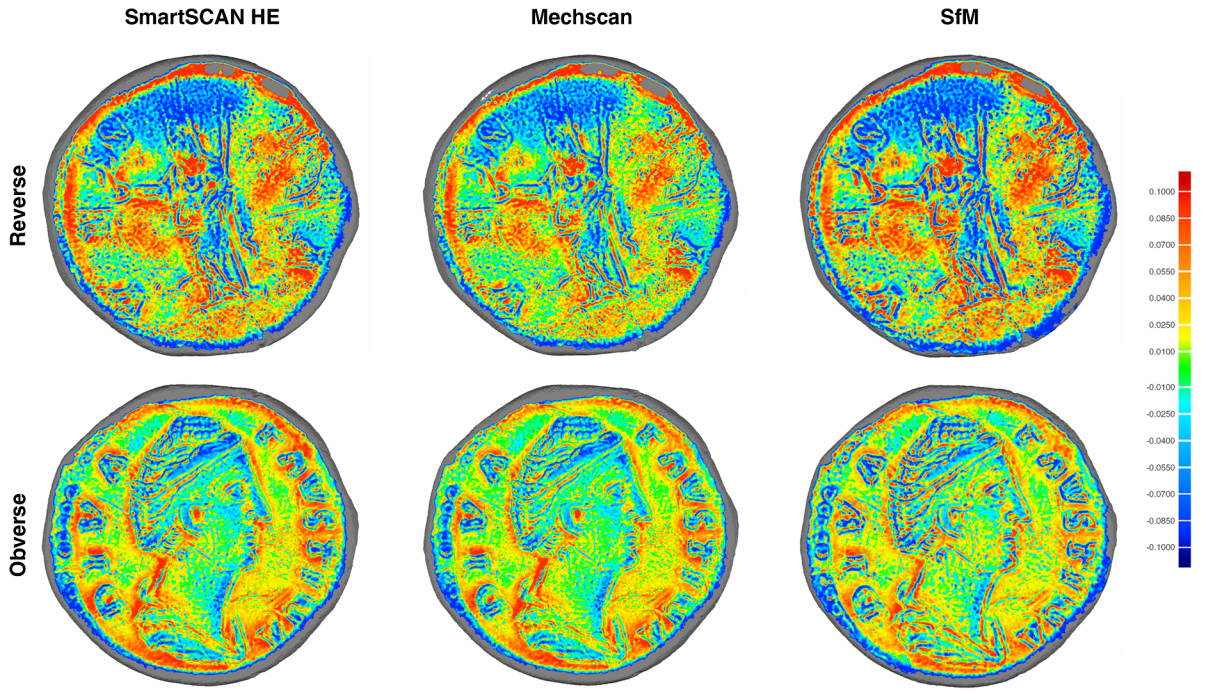

Fig. 25 Color deviation maps from pairwise comparison of DEM with 3-D models of obverse and reverse of coin B.

geometrical characteristics. Moreover, these differences can be explained by the fact that all geometrical measurements depend intrinsically on the resolution, accuracy, and precision of the systems and techniques themselves and of the acquired data, besides the sources of error. Although the obverse of coin A presents the best results in the 3-D data comparison, showing a higher percentage of similar points, it is interesting to observe how the same technique registered differently each face of the two coins. Issues related to the intrinsic characteristics of the material of the coins (i.e., silver alloy), including reflectivity properties of the material's surface, should be considered.

Even if they may not be representative of the possible highest quality outcome of the systems used, the 3-D models

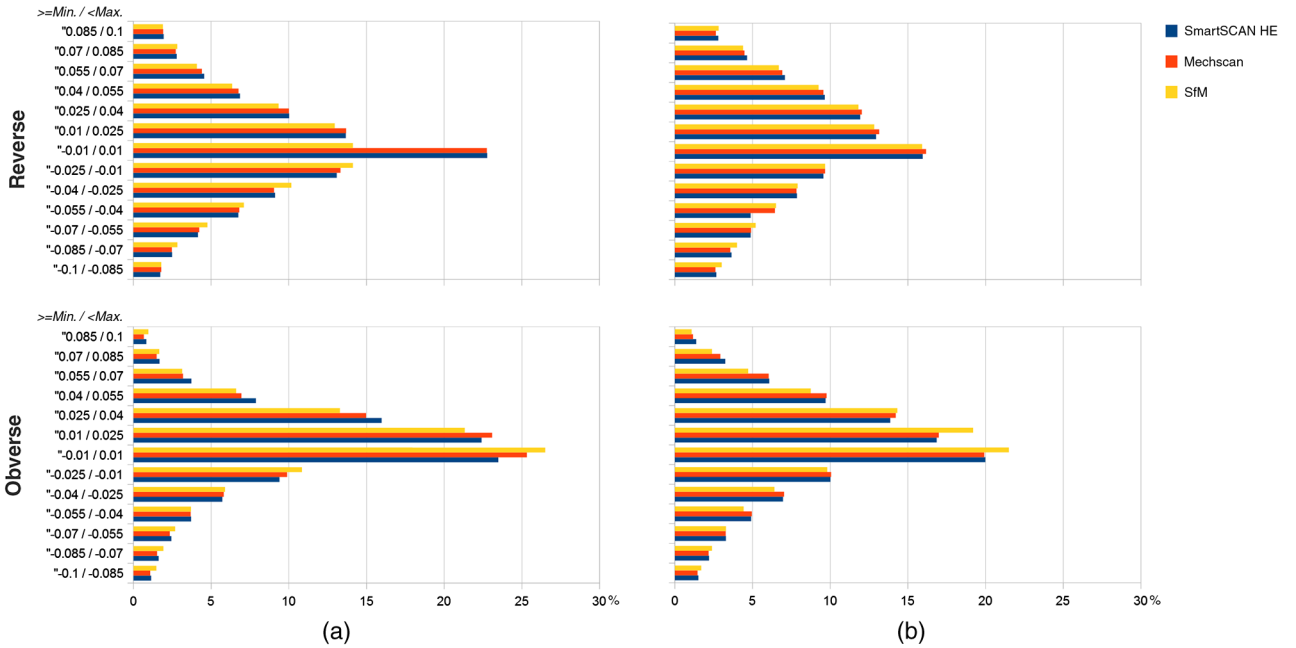

Fig. 26 Deviation distribution of points for reverse and obverse of coins (a) and (b).

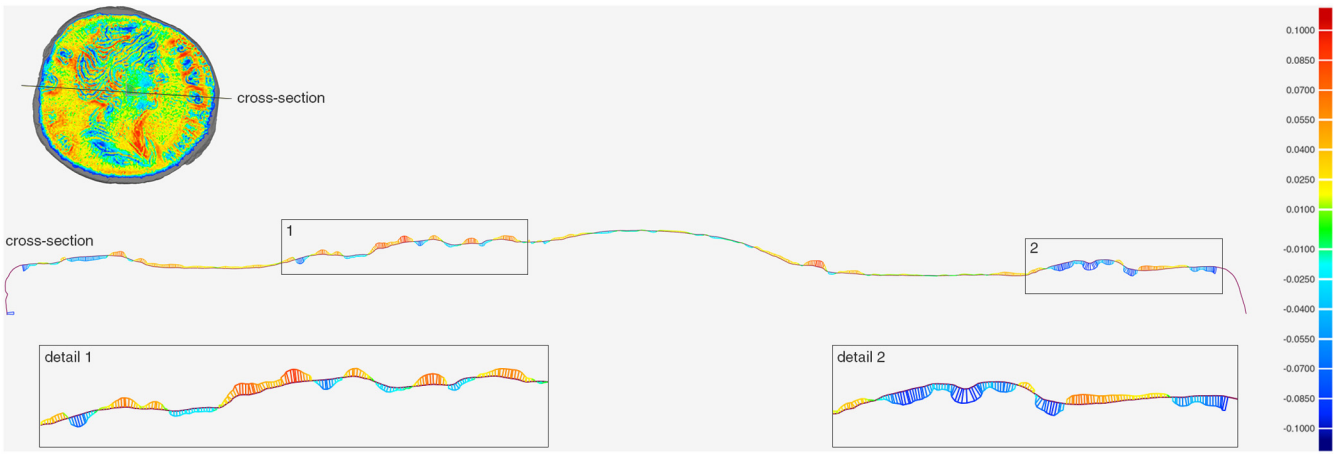

Fig. 27 A cross-section of coin A is shown here as an example of the deviation in height between SmartSCAN HE (granate line) and DEM (color deviation map, from red to dark blue). Inset 1 shows an enlarged detail of the profile of the hair, whereas inset 2 shows an enlarged detail of the profile of one of the letters.

acquired by both SLSs (i.e., SmartSCAN and Mechscan) exhibit finer geometrical details than SfM. As previously mentioned, the smallest feature expected to be identified by the SmartSCAN scanner would be 40 μm (no information available for Mechscan). The SmartSCAN system has values according to standard procedures for estimation of accuracy,[42] and any deviation from these certified 3-D scanners should be considered real at a certain value and may be used to evaluate the accuracy of the 3-D models acquired by the other systems and techniques.

The results of the obverse of coin A indicate a higher similarity between SfM and DEM, whereas on the remaining three faces, the overall results between the 3-D reference models and the DEM are not dramatically different. These results are rather unexpected if we take into account the topological data of the 3-D models (see Table 4), because SfM has the smallest number of points (e.g., 200,002 for coin A, while SmartSCAN has 540,191 and Mechscan 1,342,685 points), potentially resulting in fewer fine details. These characteristics may also help to explain the differences in the final size and other measurements of the coins.

Regarding the fine morphology of the photometric imaging technique, leading to the DEM, the photographic acquisition resolution was 13 μm (in both X and Y), and this was combined with the data at 100-μm resolution from the laser scanner. The DEM (later filtered) took the median of the multiple scanner Z coordinates values; it was also necessary to perform scaling and registration of images (including normalizing the radius, which varied $\pm 7\%$), as well as calculation of surface normals (using regression over a subset of the

intensity distribution) and spatial alignment to the nearest pixel. As with all image-based modeling,[43] this sequence of steps might generate some "irreversible" changes in the morphology of the surface of the digital representation of the coins, which could thereafter add distortion and computational artifacts when combining low with high spatial frequencies.

It is common that from the 3-D data acquisition stage through the postprocessing stage to the final export of the 3-D model (Fig. 22), some geometric changes are likely to occur. As each stage of the process depends on the outcome of the previous stages and determines the following ones, all parameters and procedures must be tailored accordingly. Certain 3-D data acquisition and postprocessing techniques (e.g., subsampling, noise reduction, smoothing and other filters, filling holes, mesh decimation, compression) may conceal, distort, or eliminate relevant data—if not at a macro level, at least at a micro level. Moreover, the algorithms used for processing data may differ between software and within versions, eventually yielding distinct results. Thus, we may ask how accurate is the captured data in respect to the original object? And how will this level of accuracy affect the analysis, classification, and interpretation of the CH object? These issues make it no longer possible to distinguish clearly between "raw" measured data and "invented" data, leading to loss of authenticity of the model and erroneous interpretations.[39,40,44] This also emphasizes the importance of linking metadata, paradata, and other meaningful information to the data when populating the archival record.[40]

5 Conclusions

This study has demonstrated that photometric image data can be combined successfully with laser scanner data to produce a DEM that has the best characteristics of both the geometric accuracy of the laser scanner with the fine detail and realistic color of the imagery from the camera. The increase in spatial resolution in this case was substantial: from 10 pixels/mm (100 μm) for the laser scanner to 75 pixels/mm (13 μm) for the camera. By transforming the two sets of surface gradients into the Fourier domain and balancing their relative power, the blending was controlled to minimize distortion and computational artifacts in the final 3-D surface. In effect, the photometric detail was able to modulate the smooth underlying form of the object, akin to texture mapping in computer graphic rendering.

In this study, we have also performed a topological and brief geometrical characterization and analysis of the 3-D digital models acquired by different 3-D systems and techniques. Furthermore, we compared the results between the 3-D data of each coin, in order to evaluate the different types of systems and techniques used for numismatic studies and general dissemination.

The type of analysis described herein helped to confirm that the spatial resolution of the specific system used to acquire 3-D data leads, as expected, to differences both in the overall and in the fine morphology of the coins. Moreover, different resolutions, among other issues, may reveal, distort, or conceal topographical details of the surface. This issue is of great importance when analyzing and interpreting variations in spatial features. Basic geometric and other measurements (e.g., maximum diameter, area, volume, weight, density) and advanced measurements were undertaken and shape factor was also computed.

One of the things that make the Faustina coinage unique is that her designs evolved over 20 years and show great typological and morphological variety, as exemplified by the two coins in the present study. Although we have attempted to characterize the coins, we are well aware that these measurements are not very meaningful per se if they are not contextualized and compared with other coins or relevant data. Changes over time of such features would naturally require a larger dataset.

Despite the fact that the DEM (as well as the SfM) model did not reach the highest quality of the 3-D data acquired by SLSs, the photometric imaging technique should be considered as an additional and alternative technique for producing 3-D models for visualisation purposes. In any case, depending on the characteristics of the object, the scale of observation, and the type of information required, the accuracy, resolution, and precision of the measurements should be high enough to fulfill the numismatist's needs for an improved scientific documentation and study of coins. Although a 3-D digital model does not provide a complete representation of the object, it should be understood as a powerful tool, potentially with valid data, for CH research that is complementary to other measurement techniques and fields of knowledge.[40] After all, this is the multidisciplinary nature of CH objects.

In this study, new research approaches to digital imaging have been shown to complement traditional techniques, not to replace them. Current ongoing research and development will soon enable automatic digitization of collections in heritage institutions with large quantities of objects, such as coin hoards, creating a 3-D representation of each object or coin "in the round." This will allow digital systems and digital archives to be populated with 3-D data, thereby enabling analysis and visualization of both individual objects and groups of objects. If the procedure proposed herein could be automated, with an image processing pipeline, it would be a valuable alternative technique to obtain 3-D models of large numbers of coins in collections.

Acknowledgments

This research study has been conducted jointly with the 3DIMPact research group (3-D Imaging, Metrology & Photogrammetry Applied Coordinate Technologies) at UCL CEGE. It was carried out under the auspices of the European COST Action TD1201 Color and Space in Cultural Heritage (COSCH). Thanks to Dr. Anna Bentkowska-Kafel for providing the coins and making them available for photography and 3-D and analytic imaging, as well as to Dr. Dirk Rieke-Zapp, from AICON 3-D Systems GmbH, and Aurore Mathys, from the Royal Belgian Museum of Natural Sciences (RBINS), for providing their 3-D digital models of the coins. The COSCH project website is at www.cosch.info. The images and 3-D datasets of the Roman Coins project and associated reports can be accessed through Ref. 41.

References

1. M. Beckmann, *Diva Faustina: Coinage and Cult in Rome and the Provinces, Study 26*, American Numismatic Society, New York (2012).
2. R. P. Duncan-Jones, "Crispina and the coinage of the empresses," *Numis. Chron.* **166**, 223–228 (2006).
3. H. Mattingly, "The consecration of Faustina the elder and her daughter," *Harv. Theological Rev.* **41**(2), 147–151 (1948).

4. C. Rowan, "Imaging the golden age: the coinage of Antoninus Pius," *Pap. Br. Sch. Rome* **81**, 211–246 (2013).
5. E. Pye, *Caring for the Past: Issues in Conservation for Archaeology and Museums*, p. 103, James & James, London, United Kingdom (2001).
6. T. Malkogeorgou, "The ethics of conservation practice: a look from within," *V&A Conserv. J.* **52**, 9–11 (2006).
7. H. Mara et al., "Ancient coins and ceramics–3D and 2D documentation for preservation and retrieval of lost heritage," in *Proc. 2nd ISPRS Intl. Workshop 3D-ARCH: 3D Virtual Reconstruction and Visualization of Complex Architectures*, pp. 12–13 (2007).
8. M. Mudge et al., "Reflection transformation imaging and virtual representations of coins from the Hospice of the Grand St. Bernard," in *Proc. 6th Intl. Symp. on Virtual Reality, Archaeology and Cultural Heritage (VAST), Pisa*, Eurographics Association, Geneva, pp. 29–39 (2005).
9. C. J. Howgego, "The potential for image analysis in numismatics," Chapter 11 in *Images and Artefacts of the Ancient World*, A. K. Bowman and M. Brady, Eds., pp. 109–113, British Academy, London, United Kingdom (2005).
10. G. Hoberman, *The Art of Coins and their Photography*, pp. 340–342, Lund Humphries, London, United Kingdom (1981).
11. A. Hawkins and D. Avon, *Photography: The Guide to Technique*, pp. 229–231, Blandford Press, Poole (1979).
12. M. Goodman, *Numismatic Photography*, 2nd ed., pp. 49–54, Zyrus Press, Irvine, California (2009).
13. J. Hedrich et al., "Image-based comparison of pre-modern coins and medals," in *Farbworkshop*, pp. 156–169, University of Koblenz (2010).
14. S. Zambanini et al., "Historical coins in 3D: acquisition and numismatic applications," in *Proc. 10th Intl. Symp. on Virtual Reality, Archaeology and Cultural Heritage (VAST), Malta*, Eurographics Association, Geneva, pp. 49–52 (2009).
15. M. Kampel, R. Huber-Mork, and M. Zaharieva, "Image-based retrieval and identification of ancient coins," *IEEE Intell. Syst.* **24**(2):26–34 (2009).
16. M. Zaharieva et al., "On ancient coin classification," in *Proc. Intl. Symp. Virtual Reality, Archaeology and Cultural Heritage (VAST), Brighton*, Eurographics Association, Geneva, pp. 55–62 (2007).
17. M. Reisert, O. Ronneberger, and H. Burkhardt, "A fast and reliable coin recognition system," in *Joint Pattern Recognition Symp.*, pp. 415–424, Springer, Berlin (2007).
18. O. Arandjelovic, "Automatic attribution of ancient Roman imperial coins," in *Proc. IEEE Computer Vision and Pattern Recognition Conf.*, pp. 1728–1734 (2010).
19. R. Huber-Mörk et al., "Identification of ancient coins based on fusion of shape and local features," *Mach. Vision Appl.* **22**(6), 983–994 (2011).
20. L. J. van der Maaten and P. Poon, "Coin-o-matic: a fast system for reliable coin classification," in *Proc. Muscle CIS Coin Competition Workshop*, Berlin, Germany, pp. 7–18 (2006).
21. V. Moitinho de Almeida, "Towards functional analysis of archaeological objects through reverse engineering processes," PhD Thesis, Department of Prehistory, Facultat de Filosofia i Lletres, UAB (2013).
22. M. Hess, "Online survey about current use of 3D imaging and its user requirements in cultural heritage institutions," in *Proc. Int. Congress on Digital Heritage*, Granada, Spain, Vol. 2, pp. 333–338 (2015).
23. L. Hannan, H. J. Chatterjee, and R. Duhs, "Object based learning: a powerful pedagogy for higher education," in A. Boddington, J. Boys, and C. Speight, Eds., *Museums and Higher Education Working Together*, pp. 159–168, Ashgate, Farnham (2013).
24. M. Hödlmoser et al., "Evaluation of historical coin 3D models," in *Proc. Conf. on Comp. Applications and Quantitative Methods in Archaeology (CAA)*, Granada (2010).
25. L. W. MacDonald, "The limits of resolution," in *Proc. BCS Conf. on Electronic Visualisation and the Arts (EVA)*, London, pp. 149–156 (2010).
26. T. Malzbender, D. Gelb, and H. Wolters, "Polynomial texture maps," in *Proc. ACM Siggraph*, Vol. 28, pp. 519–528 (2001).
27. J. Happa et al., "Illuminating the past– state of the art," in *Proc. 10th Intl. Symp. on Virtual Reality, Archaeology and Cultural Heritage*, Malta (2009).
28. G. Earl, K. Martinez, and T. Malzbender, "Archaeological applications of polynomial texture mapping: analysis, conservation and representation," *J. Archaeol. Sci.* **37**(8), 2040–2050 (2010).
29. G. Palma et al., "Telling the story of ancient coins by means of interactive RTI images," in *Proc. Conf. on Comp. Applications and Quantitative Methods in Archaeology (CAA)*, Southampton, pp. 177–185 (2012).
30. L.W. MacDonald, A. H. Ahmadabadian, and S. Robson, "Determining the coordinates of lamps in an illumination dome," *Proc. SPIE* **9528**, 95280I (2015).
31. P. Bourke, "Calculating the area and centroid of a polygon" 1988, www.seas.upenn.edu/~sys502/extra_materials/Polygon%20Area%20and%20Centroid.pdf (3 December 2016).
32. L. W. MacDonald, "Surface reconstruction from photometric normals with reference height measurements," *Proc. SPIE* **9527**, 952706 (2015).
33. R. T. Frankot and R. Chellappa, "A method for enforcing integrability in shape from shading algorithms," *IEEE Trans. Pattern Anal. Mach. Intell.* **10**(4), 439–451 (1988).
34. S. Tominaga, H. Ujike, and T. Horiuchi, "Surface reconstruction of oil paintings for digital archiving," in *Proc. IEEE Southwest Symp. on Image Analysis & Interpretation*, pp. 173–176 (2010).
35. J.-A. Beraldin, "Integration of laser scanning and close-range photogrammetry– the last decade and beyond" 2004, http://www.isprs.org/proceedings/XXXV/congress/comm5/papers/188.pdf (3 December 2016).
36. W. Boehler et al., "Investigating laser scanner accuracy," in *Proc. 19th CIPA Symp.*, Antalya (2003).
37. A. Georgopoulos, C. Ioannidis, and A. Valanis, "Assessing the performance of a structured light scanner," in *ISPRS Int. Archives of Photogrammetry, Remote Sensing and Spatial Information Sciences*, Newcastle upon Tyne, Vol. 38, pp. 250–255 (2010).
38. Joint Committee for Guides in Metrology, "JCGM 100:2008. Evaluation of measurement data–guide to the expression of uncertainty in measurement (GUM)" (2008).
39. S. Havemann, "Intricacies and potentials of gathering paradata in the 3D modelling workflow," in *Paradata and Transparency in Virtual Heritage*, A. Bentkowska-Kafel, H. Denard, and D. Baker, Eds., pp. 145–162, Ashgate Publishing (2012).
40. V. Moitinho de Almeida, "Metadata and Paradata record template," in *COSCH Case Study of Roman Silver Coins Using Spectroscopic and 3D Imaging Approaches*, Internal document. COST Action TD-1201 (2015).
41. https://coschromancoins.wordpress.com.
42. VDI/VDE, VDI/VDE 2634– part 2:20112-08, *Optical 3D Measuring Systems—Optical Systems Based on Area Scanning*, VDI, Beuth Verlag, Berlin (2012), http://www.vdivde-it.de/.
43. F. Remondino and S. F. El-Hakim, "Image-based 3D modeling: a review," *Photogramm. Rec.* **21**, 269–291 (2006).
44. V. Moitinho de Almeida and J. A. Barceló, "3D scanning and computer simulation of archaeological artefacts," in *Proc. 1st Intl. Conf. on Best Practices in World Heritage: Archaeology*, Menorca, pp. 384–399 (2012).

Lindsay Macdonald is a research fellow in the 3DIMPact research group in the UCL Faculty of Engineering Sciences, visiting professor at the University of Westminster, and a fellow of five professional societies including IS&T. His BSc (physics) and BEng (electronics) degrees were from the University of Sydney and his PhD (image science) from UCL. He has authored over 120 papers and edited eight books on color image science and its application to cultural heritage.

Vera Moitinho de Almeida is a postdoctoral researcher at the Quantitative Archaeology Lab (LAQU-UAB) and member of AGREST research group. She obtained PhD from UAB, focusing on functional analysis of archaeological objects, using 3-D digital models and reverse engineering processes. She has MSc in prehistoric archaeology (UAB), an MSc in multimedia technologies (FEUP), and BA in fine arts (IPC). She has authored more than forty papers and book chapters in 3-D applications in cultural heritage.

Mona Hess is a research associate at UCL CEGE's 3DIMPact research group. She holds a degree in architecture from Technical University Munich, MA in heritage conservation from University of Bamberg, and PhD in 3-D imaging metrology for cultural heritage from UCL. She has more than 10 years of experience in cross-disciplinary international 3-D imaging projects and is specialized in 3-D close-range recording for cultural heritage and conservation science, including curatorship of 3-D digital museum collections.